ADVANCED MATERIALS INTERFACES Open Access
www.advmatinterfaces.de

Check for updates

Revealing Low Thermal Conductivity of Germanium Tin Semiconductor at Room Temperature

*Sabur Ayinde and Maksym Myronov**

The low thermal conductivity of a material is a key essential parameter for its potential application in high-performance thermoelectric devices. Unprecedently low thermal conductivity of germanium tin ($Ge_{1-x}Sn_x$) semiconductor thin film is experimentally obtained at room temperature. The thermal conductivity decreases with increasing Sn concentration in the relaxed $Ge_{1-x}Sn_x$ binary alloy, which is explained mainly by increasing the interatomic distance between atoms via alloying. A pronounced decrease of thermal conductivity, by over 20 times, from 58 W $m^{-1}K^{-1}$ in Ge to ≈2.5 W $m^{-1}K^{-1}$ in relaxed $Ge_{1-x}Sn_x$, with Sn content up to 9% is observed. This thermal conductivity is just ≈2 times higher than that of the state-of-the-art thermoelectric material, Bismuth Selenium Telluride. $Ge_{1-x}Sn_x$, in contrast, is a non-toxic Group-IV semiconductor material, that is epitaxially grown on a standard silicon wafer up to 300 mm diameter using the semiconductor industry standard epitaxial growth technique. As a result, it can lead to the creation of a long-awaited high-performance low-cost thermoelectric energy generator for room-temperature applications in human's daily life and would make a substantial contribution toward global efforts in CO_2 emission-free and green electricity generation.

1. Introduction

Thermoelectric (TE) technology has the potential to play a significant role in meeting the growing demand for sustainable and renewable energy sources. A large percentage of global energy use comes from fossil fuels, which contribute to the increase of waste heat released to the environment. As a result, thermoelectricity has received much attention with the ideas revolving around improving its efficiency.[3–5] The demand for sustainable and renewable energy is a way of finding solutions to the devastating changes in climate conditions.[2,8] Global research is ongoing to develop new and efficient thermoelectric materials.[3,5] Advances in nanotechnology and materials synthesis have shown the possibilities to substantially improve the performance of TE materials by various approaches centered on reducing thermal conductivity while maintaining high electrical conductivity. Thermoelectricity has several advantages over other energy conversion technologies: devices need no moving parts, and they emit no noise and no pollution. TE devices are highly reliable and have a long lifespan. Current thermoelectric materials, however, have low efficiency and are not suitable for widespread commercial use.[9]

Thermoelectricity is the direct conversion of heat to electricity or electricity into heat via two related mechanisms, the Seebeck and the Peltier effects.[10] The Seebeck effect refers to the generation of an electrical voltage across a material due to a temperature difference across two ends of the material. The Peltier effect on the other hand is the generation or absorption of heat when an electric current flows through a material. The performance of a TE material is characterized by a dimensionless quantity (ZT) known as the figure of merit (ZT) and is defined as

$$ZT = \frac{S^2}{k}\sigma T \tag{1}$$

where S is the Seebeck coefficient, σ is the electrical conductivity, k is the thermal conductivity, and T is the absolute temperature. A large ZT value indicates thermoelectric material with high efficiency, in converting heat to electricity. It is clear from Equation (1) that low thermal conductivity, high Seebeck coefficient, and high electrical conductivity are essential to maximize ZT at a given temperature.[11] The Seebeck coefficient of 3D or bulk material is defined as

$$S = \frac{8\pi^2 k_B^2}{3eh^2} m^* T \left(\frac{\pi}{3n}\right)^{2/3} \tag{2}$$

where m^* is the effective mass of the charge carrier, electron, or hole, and n is the electron charge carrier density (p for holes), k_B is the Boltzmann constant, e is the electron charge and h is the

S. Ayinde, M. Myronov
Department of Physics
University of Warwick
Coventry CV4 7AL, UK
E-mail: M.Myronov@warwick.ac.uk

The ORCID identification number(s) for the author(s) of this article can be found under https://doi.org/10.1002/admi.202300711

© 2023 The Authors. Advanced Materials Interfaces published by Wiley-VCH GmbH. This is an open access article under the terms of the Creative Commons Attribution License, which permits use, distribution and reproduction in any medium, provided the original work is properly cited.

DOI: 10.1002/admi.202300711

© 2023 The Authors. Advanced Materials Interfaces published by Wiley-VCH GmbH

21967350, 0, Downloaded from https://onlinelibrary.wiley.com/doi/10.1002/admi.202300711 by Test, Wiley Online Library on [07/12/2023]. See the Terms and Conditions (https://onlinelibrary.wiley.com/terms-and-conditions) on Wiley Online Library for rules of use; OA articles are governed by the applicable Creative Commons License

Plank constant. Electrical conductivity, σ, is proportional to the carrier density and mobility, μ, defined as,

$$\sigma = ne\mu \tag{3}$$

Carrier density, n, is a tuning parameter in the sense that an increase in n causes a drop in carrier mobility. This leads to a rise in electrical conductivity, but at the same time, it reduces the Seebeck coefficient. This is the most important challenge in thermoelectricity, the difficulty to significantly enhancing ZT of any thermoelectric material. It is however possible to improve the ZT performance of a material by minimizing its thermal conductivity. Thermal conductivity of a material consists of electronic and phononic components, as follows:

$$k = k_e + k_l \tag{4}$$

The electronic component, k_e is a function of heat transfer by the charge carriers, while the phononic component, k_l, is a measure of heat transferred through lattice vibrations or phonons. Another obstacle in the way is the interdependence of electrical and thermal conductivity due to which most efforts have been directed toward the suppression of the phononic component of the thermal conductivity k_l. This has been achieved by defect engineering, crystal dislocations[12] phonon anharmonicity,[13,14] entropy engineering[15] band convergence modification[16] and microstructure engineering.[17] Thermal conductivities of elementary materials in group IV semiconductors, such as Silicon (Si), Germanium (Ge), Carbon (C), or tin (Sn)[1] are high at around room-temperature, in comparison to the most efficient TE material Bismuth Selenium Telluride ($Bi_{0.7}Sb_{0.3}Te$)[4] However, their electric properties are superior,[18–21] and they are abundant, non-toxic, and low cost, all of which make them attractive candidates for large-scale production. Their compatibility with complementary metal-oxide-semiconductor (CMOS) and ultra-large-scale integration (ULSI) is an added advantage, as those technologies are widely used in the semiconductor industry.[22,23]

In this study, we synthesized, via epitaxial growth, monocrystalline relaxed $Ge_{1-x}Sn_x$ thin film epilayers, with Sn contents up to 9%, on underlying Si substrate via a relaxed Ge buffer layer. We demonstrate, through experiments, that these $Ge_{1-x}Sn_x$ epilayers exhibit the lowest thermal conductivity value among all group-IV semiconductors, at room temperature; which happens to be comparable to one of the best TE materials and we expect that it could be lowered even further.

2. Results and Discussion

2.1. Structural Properties

Epitaxially grown $Ge_{1-x}Sn_x$/Ge/Si (001) heterostructures were characterized by a combination of techniques including high-resolution X-ray diffractometry (HR-XRD), cross-sectional transmission electron microscopy (XTEM) and scanning electron microscopy (SEM) to obtain information about the state of strain in each epilayer, Sn content in the intentionally undoped $Ge_{1-x}Sn_x$ alloy, the epilayer's thickness, density of defects, and images of micro-fabricated wires. **Figure 1** shows results of the $Ge_{1-x}Sn_x$/Ge/Si(001) heterostructure characterization by HR-XRD; with ω−2Θ scan (as in Figure 1a) containing peaks originated from Si(001) substrate at 34.56°, Ge buffer epilayer at 33.04°, while those of Ge_{1-x} Sn_x at 5% and 9% Sn content are at 32.64° and 32.15° , respectively. A shoulder peak from $Ge_{1-x}Sn_x$ epilayer with 9% Sn content is visible with a Bragg's angle at 32.38° (Figure 1a) and that corresponds to an epilayer with 7% Sn content; and could be related to strain relaxation of the epilayer. During growth, Sn content increased gradually as the layer relaxes, with an initial thinner layer of 7% Sn content. The intensity of the Si substrate peak is the highest due to its thickness of ≈600 µm, while the $Ge_{0.95}$ $Sn_{0.05}$ epilayer peak (as in Figure 1a) is the lowest due to a thickness of just ≈300 nm lower than the ≈600 nm of the Ge buffer layer. Our $Ge_{1-x}Sn_x$/Ge/Si (001) heterostructures have the same Bragg peak positions (ω−2Θ) for Si and Ge, while the Bragg peak position for $Ge_{1-x}Sn_x$ epilayer is subject to the change in the amount of Sn content in $Ge_{1-x}Sn_x$ epilayer. The in-plane and out-plane lattice constants ($a_{||}^{Ge_{1-x}Sn_x}$ and $a_{\perp}^{Ge_{1-x}Sn_x}$), and the degree of relaxation in $Ge_{1-x}Sn_x$ epilayer at 5% Sn content was obtained from the analysis of symmetric (004) and asymmetric (224) HR-XRD reciprocal space maps (RSM), shown in Figure 1b,c, with those of 9% Sn content presented in the experimental section (Figure 5). The $Ge_{1-x}Sn_x$ epilayers exhibit ≈80% degree of relaxation.

We note that the incorporation of Sn into the Ge lattice yields a larger lattice constant compared to the single element of Ge. The thickness of each $Ge_{1-x}Sn_x$/Ge/Si (001) epilayer was obtained by analyzing the dark field and bright field images obtained from XTEM, as presented in Figure 1c,d. High density of misfit dislocations is clear at the Ge/Si interface due to the lattice mismatch of 4.17%, as reported elsewhere.[24] The additional 111 plane into the lattice structure of the relaxed $Ge_{0.95}$ $Sn_{0.05}$ epilayer, seen in Figure 1f, is a Lomer dislocation (an edge-like dislocation), which tends to induce relaxation in $Ge_{1-x}Sn_x$ epilayer.[25–27] Meanwhile, the $Ge_{1-x}Sn_x$ at 5% Sn content has a lattice mismatch of ≈0.7%, with respect to relaxed Ge buffer epilayer, and that increases to ≈1.3% for the alloy with 9% Sn content. As Sn concentration increases, so does the out-of-plane lattice constant until the epilayer reaches critical thickness, allowing relaxation through the generation of dislocations. Consequently, the dislocation density is proportional to the amount of lattice mismatch strain in the epilayer. However, there is not sufficient evidence to say that all dislocations reach the $Ge_{1-x}Sn_x$ surface. The threading dislocation density (TDD) in the Ge buffer layer is estimated to be ≈4.7 × $10^6 cm^{-2}$, in agreement with previous reports.[28,29] The TDD in $Ge_{1-x}Sn_x$ at 5% and 9% are estimated to be ≈7.0 × $10^6 cm^{-2}$and ≈9.5 × $10^6 cm^{-2}$, respectively, as obtained from XRD coupled scan analysis using Debye Scherrer formula.[30] Paul et al reported, through their theoretical physical simulations that the thermal conductivity of some group IV materials (p-channel $Si_{1-x}Ge_x$, Si, and Ge quantum well) remains relatively stable at threading dislocation densities <$10^{10} cm^{-2}$ [31] This indicates that the low dislocation density observed in our relaxed $Ge_{1-x}Sn_x$ epilayers cannot be responsible for the significant reduction in the thermal conductivity of the material.

© 2023 The Authors. Advanced Materials Interfaces published by Wiley-VCH GmbH

21967350, 0, Downloaded from https://onlinelibrary.wiley.com/doi/10.1002/admi.202300711 by Test, Wiley Online Library on [07/12/2023]. See the Terms and Conditions (https://onlinelibrary.wiley.com/terms-and-conditions) on Wiley Online Library for rules of use; OA articles are governed by the applicable Creative Commons License

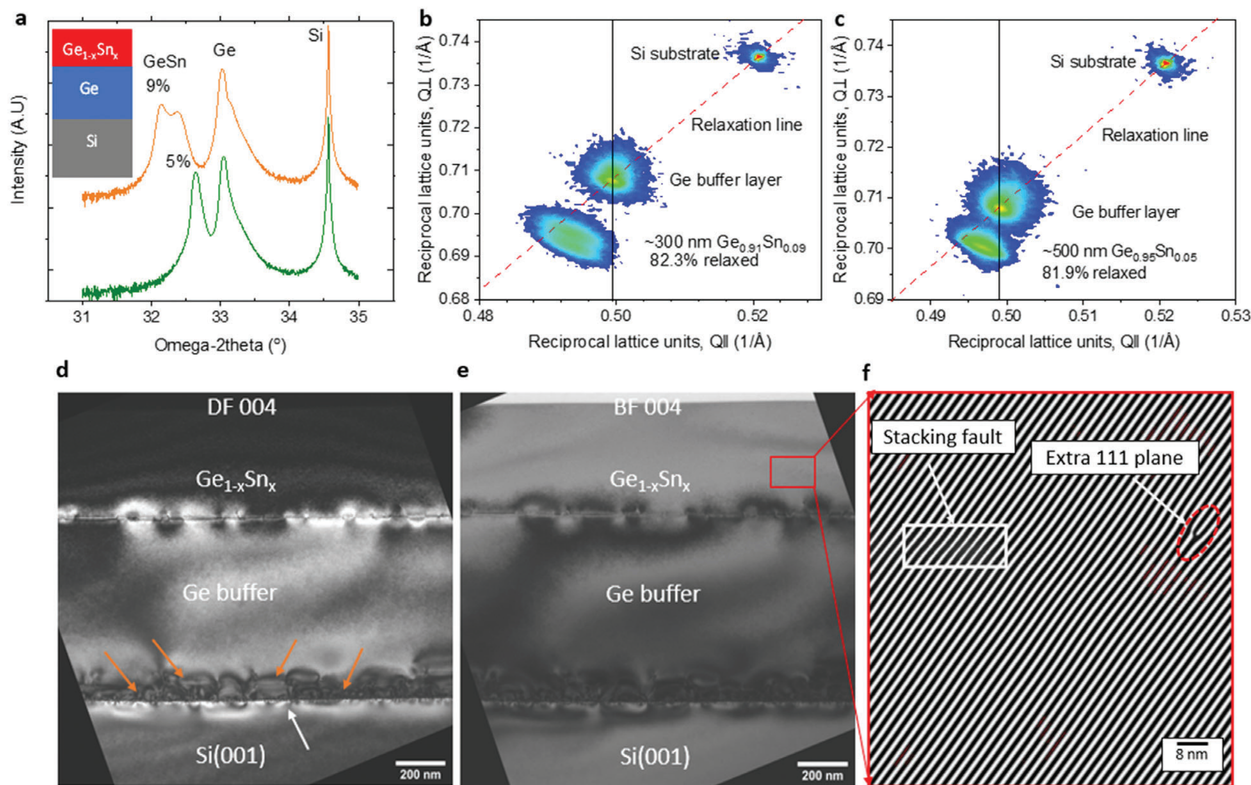

Figure 1. Results of $Ge_{1-x}Sn_x$/Ge/Si heterostructures characterization by HR-XRD and XTEM. a) HR-XRD ω-2Θ scans of relaxed $Ge_{0.95}Sn_{0.05}$/Ge/Si heterostructure, b) the symmetric (004) and c) the asymmetric (224) HR-XRD RSMs showing the degree of relaxation of $Ge_{0.95}Sn_{0.05}$ epilayers. d) XTEM dark field (DF) image of relaxed $Ge_{0.95}Sn_{0.05}$ sample along the 004 direction, with the arrows showing the interfacial defect at the Si/Ge interface and their propagation, due to their lattice mismatch, and e) its equivalent bright field (BT) image of the relaxed thin film along 004 plane. f) The inverse Fast Fourier Transform (FFT) filtering pattern image of relaxed $Ge_{0.95}Sn_{0.05}$ sample from High Resolution (HR) lattice imaging analysis with the red oval dotted line showing an additional 111 plane and the white rectangular shaped portion showing slight stacking fault in the lattice structure.

2.2. Raman Spectra

Typical Raman spectra of $Ge_{1-x}Sn_x$/Ge/Si heterostructures, obtained at room temperature, are shown in **Figure** 2a, with ω_{Ge-Ge} Raman shift peaks at 297.38 cm^{-1} and 293.12 cm^{-1} corresponding to Ge-Ge modes originated from $Ge_{1-x}Sn_x$ epilayers with Sn content at 5% and 9%, respectively. Low intensity ω_{GeSn} peaks are located at 260 cm^{-1} and 256 cm^{-1} and can be compared to what was obtained elsewhere.[32] Low Sn contents of $Ge_{1-x}Sn_x$ epilayers have given rise to high intensity of ω_{Ge-Ge} vibration mode peaks from the $Ge_{1-x}Sn_x$ epilayer in the Raman spectra of samples; and so this mode peak was used in subsequent measurements. A shift to lower cm^{-1} number in $Ge_{1-x}Sn_x$ peaks for the 9% Sn content compared to the sample at 5% Sn content was observed, which is usually identified by the peak analyzer using appropriate software. The shift in the Raman peak is due to higher Sn content in the relaxed $Ge_{1-x}Sn_x$ epilayer. A similar shift in the peak attributed to $Ge_{1-x}Sn_x$ epilayers has been reported elsewhere.[32]

2.3. Raman Thermometry

The temperature-dependent Raman spectra were acquired from each $Ge_{1-x}Sn_x$/Ge/Si heterostructure separately as their temperature dependencies are dissimilar (see Figure 2b). The Ge-Ge mode shifts are temperature-dependent, due to phonon interaction in the $Ge_{1-x}Sn_x$ epilayer, so they can be employed to measure variations in temperature. This variation can be used to extract the thermal conductivity of a material. A non-heating laser power density of ≈25 $kWcm^{-2}$ was applied, and a temperature monitoring sample stage was used to ensure the temperature equilibrium was reached at the sample's surface during each measurement.

The ω_{Ge-Ge} peak from the $Ge_{1-x}Sn_x$/Ge/Si heterostructures decreases linearly with the increase in temperature at the surface of material (Figure 2b), indicating an increase in the lattice constant with the temperature. The peak shift is due to temperature rise only and is not related to Sn content or strain in the epilayer. The slope, $\eta = \Delta\omega/\Delta T$, from the temperature dependent micro-Raman measurements is calculated to be -0.01868 ± 0.00027 cm^{-1} K^{-1} and -0.02002 ± 0.00022 cm^{-1} K^{-1} for Sn content at 5 and 9%, respectively. These values are comparable to similar reports for Ge/Si[33] and $Ge_{1-x}Sn_x$/Ge/Si[7] obtained elsewhere.

2.4. Isolation of a Single Epilayer from Multilayers

In order to measure thermal conductivity of a single epilayer, thermal isolation from substrate and other layers is necessary;

© 2023 The Authors. Advanced Materials Interfaces published by Wiley-VCH GmbH

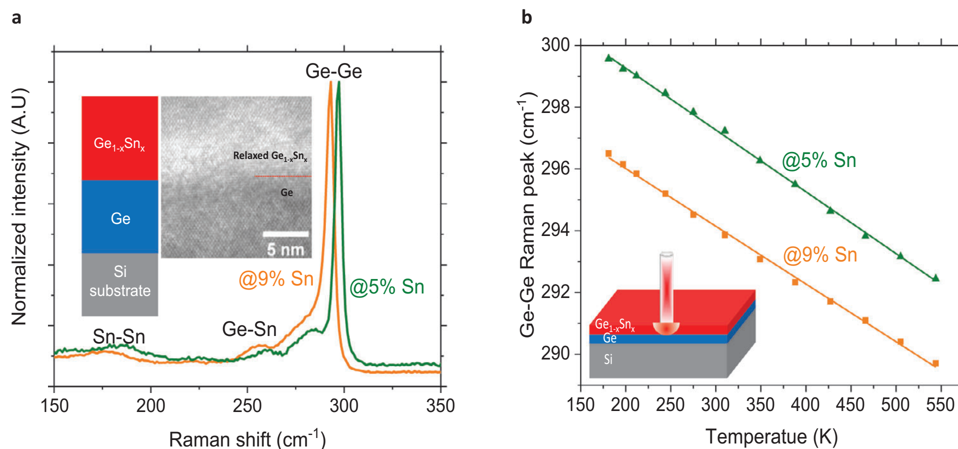

Figure 2. Raman spectra of $Ge_{1-x}Sn_x$ a) spectrum at 293 K of $Ge_{1-x}Sn_x$/Ge/Si heterostructure, showing Ge-Ge, Ge-Sn, and Sn-Sn vibration modes at 297 cm^{-1}, 261 cm^{-1} and 187 cm^{-1}, respectively for 5% Sn content, while corresponding shift in the peaks to 293.4 cm^{-1}, 256 cm^{-1} and 176 cm^{-1}.was observed with 5% Sn content. The inset shows the cross-section schematics of heterostructure (left) and an HR-TEM image of the $Ge_{0.95}Sn_{0.05}$/Ge interface region with no visible threading dislocation propagating from Ge to GeSn epilayer. b) Temperature-dependent thermometric data of bulk $Ge_{1-x}Sn_x$ /Ge/Si at Sn content of 5 and 9%. The lowest possible power density of <25 K W cm^{-2} was applied to the sample surface to obtain the temperature-dependent data to avoid overheating.

otherwise, underlayers will act as a heat sink. Isolation becomes possible by way of suspending $Ge_{1-x}Sn_x$ microwires, as shown in **Figure** 3. First, $Ge_{1-x}Sn_x$/Ge/Si microwires are patterned into the mesas, see Figure 3a. Then the surface of Si substrate underlayer was selectively removed (etched) in order to suspend $Ge_{1-x}Sn_x$/Ge epilayers (Figure 3b). Finally, Ge was selectively etched to completely suspend $Ge_{1-x}Sn_x$ epilayer (Figure 3c), as verified by SEM imaging (Figure 3e,f), and the appearance of the etch pit after release (Figure 3g). Thermal isolation of $Ge_{1-x}Sn_x$ epilayers is essential for all subsequent measurements of thermal conductivity, as this step is crucial in eliminating any parasitic thermal effects, from other epilayers or the substrate.[34] Therefore, an optimized thermoelectric device structure[8] is required in order to minimize thermal losses in the device and to increase its efficiency. Hence, our microfabrication approach to obtain such a novel $Ge_{1-x}Sn_x$ thermoelectric device structure is shown in Figure 3c.

2.5. Thermal Conductivity

Thermal conductivity was extracted from Raman spectra, obtained from non-suspended $Ge_{1-x}Sn_x$/Ge/Si heterostructures, as well as suspended $Ge_{1-x}Sn_x$/Ge heterostructure, and suspended $Ge_{1-x}Sn_x$ microwires. Our analysis is based on the radial Gaussian heat distribution model.[35–37] Thermal conductivity for each sample, at 5 and 9% Sn content, was calculated using measurements of the sample's surface temperature, $\Delta T = \Delta\omega/\eta$, obtained from temperature dependency of Ge-Ge mode shift, seen in Figure 2b. Local temperature was measured at the surface of the sample by applying the heating laser power density to cause peak shift, ignoring any wide peak shifts associated with overheating.

Figure 4 summarizes thermal conductivity at room temperature, as a function of Sn content in the $Ge_{1-x}Sn_x$ alloy, obtained in this work and those available from literature. Values of

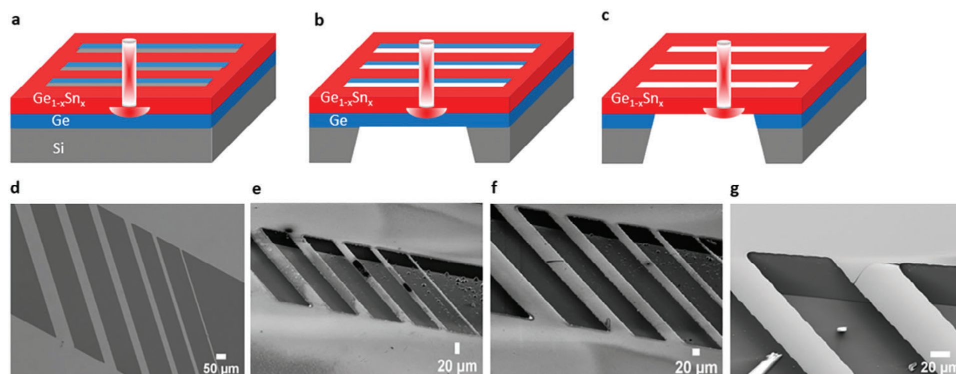

Figure 3. 3D schematics of the characterized structures and their corresponding SEM images of patterned a,d) $Ge_{1-x}Sn_x$ /Ge/Si heterostructure, b,e) suspended $Ge_{1-x}Sn_x$ /Ge and c,f) suspended $Ge_{1-x}Sn_x$ microwires. The dimensions of the microwires are 10 – 50 µm in width by 1000 µm in length. Figure 1e represents suspended $Ge_{1-x}Sn_x$ /Ge tilted by 55°, while f) shows a suspended single layer $Ge_{1-x}Sn_x$ when Ge buffer layer was selectively removed. The sample's surface and etch pit of suspended $Ge_{1-x}Sn_x$ microwires (f) are also shown in (g).

© 2023 The Authors. Advanced Materials Interfaces published by Wiley-VCH GmbH

21967350, 0, Downloaded from https://onlinelibrary.wiley.com/doi/10.1002/admi.202300711 by Test, Wiley Online Library on [07/12/2023]. See the Terms and Conditions (https://onlinelibrary.wiley.com/terms-and-conditions) on Wiley Online Library for rules of use; OA articles are governed by the applicable Creative Commons License

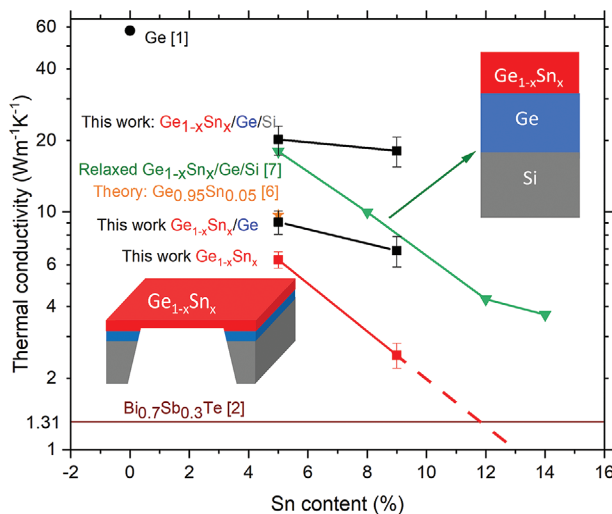

Figure 4. Summary result of Sn content dependent thermal conductivity, at room temperature, of non-suspended $Ge_{1-x}Sn_x$/Ge/Si, suspended $Ge_{1-x}Sn_x$/Ge and suspended single layer $Ge_{1-x}Sn_x$ epilayer compared to reference data of Ge[1], the most efficient TE material, $Bi_{0.7}Sb_{0.3}Te$ (brown),[2] recent report on $Ge_{0.95}Sn_{0.05}$ theoretical data (orange),[6], and relaxed bulk (green)[7] $Ge_{1-x}Sn_x$/Ge/Si. The inset shows the schematic of our suspended single-layer $Ge_{1-x}Sn_x$ microstructure (red), and the unsuspended $Ge_{1-x}Sn_x$/Ge/Si (red/blue/ash) from the reference report.[7]

20.1±2.8 and 18.2±2.6 W m^{-1} K^{-1} attributed to the unsuspended micro-fabricated $Ge_{1-x}Sn_x$/Ge/Si heterostructures microwires at 5 and 9% Sn content, respectively. When the underlayer Si material was removed, by selective etching, the thermal conductivity was reduced by more than half. Values for $Ge_{1-x}Sn_x$/Ge microwires with 5% and 9% Sn are measured to be 9.07 and 6.9 W m^{-1} K^{-1}, respectively. This is a demonstration that the parasitic thermal effect imposed by Si substrate contributes to more than ≈2 times the thermal conductivity obtained from the suspended $Ge_{1-x}Sn_x$/Ge microwire, see Figure 4. Thermal loss in the $Ge_{1-x}Sn_x$/Ge/Si heterostructure is dissipated to the highly thermally conductive Si substrate (149 W m^{-1} K^{-1}), hence substantially increasing apparent thermal conductivity. It is noted that the decreasing trend in thermal conductivity continues as the Ge buffer layer is selectively removed from $Ge_{1-x}Sn_x$/Ge, leaving the $Ge_{1-x}Sn_x$ single epilayer suspended. Similar thermal loss in the suspended $Ge_{1-x}Sn_x$/Ge epilayer was found to be dissipated to the Ge buffer layer, resulting in thermal conductivities ≈2x and ≈1.5x larger than values obtained from the suspended $Ge_{1-x}Sn_x$ epilayers at 9% and 5% Sn content, respectively.

Micro-fabrication approach (suspending the microwires) along with Sn alloying, eliminates the thermal loss in the epilayers and lowers the thermal conductivity. The Ge/Si substrate is etched, strain is released in the suspended $Ge_{1-x}Sn_x$ epilayer, and as a result, thermal losses to the buffer layer and the Si substrate are removed, thus revealing the measurement accuracy of the alloy epilayers. Due to this, monocrystalline relaxed $Ge_{1-x}Sn_x$ material exhibits extraordinarily low thermal conductivity, which has been revealed. Thermal conductivity of $Ge_{1-x}Sn_x$ in this work cannot be associated with the low density of threading dislocation (Figure 1f) or rather the misfit dislocation observed from Ge/Si and $Ge_{1-x}Sn_x$/Ge interfaces (Figure 1d), where the TDD reaching the $Ge_{1-x}Sn_x$ epilayer is minimal. The specific geometry layout in the microfabrication has helped to remove misfit dislocations and the few existing lattice distortions, and may not have contributed much to the phonon vibrations that naturally suppress the intrinsic lattice component of the thermal conductivity, k_l. According to the obtained results, we report that the phonon vibrations in the binary alloys of $Ge_{1-x}Sn_x$ increase, compared to Ge, due to Sn incorporation into the Ge lattice structure, as spacing between the neighboring atoms increases. As a result, a linear decrease in thermal conductivity down to 2.5 W m^{-1} K^{-1} with Sn content up to 9% is observed. Moreover, the linear extrapolation of obtained results can help anticipate that the thermal conductivity of $Ge_{1-x}Sn_x$ alloy could be further reduced, even lower than the best thermoelectric material ($Bi_{0.7}Sb_{0.3}Te$), to ≈1 W m^{-1} K^{-1} for Sn contents of up to 13% in a relaxed $Ge_{1-x}Sn_x$ alloy, as marked (by the dashed red lines) in Figure 4.

Thermal conductivity of the unsuspended $Ge_{1-x}Sn_x$/Ge/Si microwire at 5% Sn content, 20.1 W m^{-1} K^{-1}, is comparable to the 18 W m^{-1} K^{-1} obtained experimentally by Spirito et al from $Ge_{1-x}Sn_x$/Ge/Si heterostructures.[7] The obtained thermal conductivity of 9.1 W m^{-1} K^{-1} (as can be seen in Figure 4) for the suspended $Ge_{1-x}Sn_x$/Ge microwire at 5% Sn content, is in agreement with the 9.7 W m^{-1} K^{-1} calculated theoretically elsewhere for $Ge_{0.95}Sn._{0.05}$[6]

The incorporation of Sn into Ge lattice significantly lowers thermal conductivity of $Ge_{1-x}Sn_x$ alloy by increasing the in-plane lattice constant of the relaxed alloy and additional crystal disordering of the binary alloy. In our experiment, we vary the k_l component of the thermal conductivity only, because all epilayers are intentionally undoped. Recent studies have shown that alloying of group IV semiconductors such as Si, Ge, or Sn with other elements can significantly reduce their thermal conductivity by reducing the lattice component, k_l which can be attributed to increased crystal disorder by alloying and introduction of defects and possibly other structural changes that contribute to phonons scattering and disrupt their propagation.[6,7,38–40] As expected, the thermal conductivity in $Ge_{1-x}Sn_x$ drops with increasing Sn content from 5 to 9%, as shown in Figure 4. Similar behavior was reported by Spirito et al[7] However, a considerable difference between the thermal conductivity of the same relaxed $Ge_{1-x}Sn_x$ epilayers measured in our experiment and that reported by Spirito et al[7] is observed, and may be explained by the absence of heat loss in our suspended $Ge_{1-x}Sn_x$ epilayers. Also, our measured thermal conductivity in $Ge_{1-x}Sn_{\bar{x}}$ alloy with 5% Sn content is ≈1.5 times lower than what was recently reported theoretically by Khatami and Aksamija[6] The thermal conductivities of 2 and 1.31 W m^{-1} K^{-1} were reported elsewhere for a polycrystalline $Ge_{0.93}Sn_{0.07}$ (at 7% Sn content) and most efficient TE material ($Bi_{0.7}Sb_{0.3}Te$) that are lower than our 2.5 W m^{-1} K^{-1} obtained at 9% Sn content. It is important to note that polycrystalline materials have unstable thermal conductivity (having both in-plane and cross-plane thermal conductivity), and thus the corresponding values are relatively lower due to the high volume of defects in their planar structures. Polycrystalline materials also have poor electrical properties and therefore, are not suitable for thermoelectric applications. Finally, it is worth adding that the $Bi_{0.7}Sb_{0.3}Te$ with the lowest thermal conductivity is non-CMOS compatible, costly, and less abundant. Overall, it is apparent that an increase in Seebeck coefficient is expected from $Ge_{1-x}Sn_x$

© 2023 The Authors. Advanced Materials Interfaces published by Wiley-VCH GmbH

21967350, 0, Downloaded from https://onlinelibrary.wiley.com/doi/10.1002/admi.202300711 by Test, Wiley Online Library on [07/12/2023]. See the Terms and Conditions (https://onlinelibrary.wiley.com/terms-and-conditions) on Wiley Online Library for rules of use; OA articles are governed by the applicable Creative Commons License

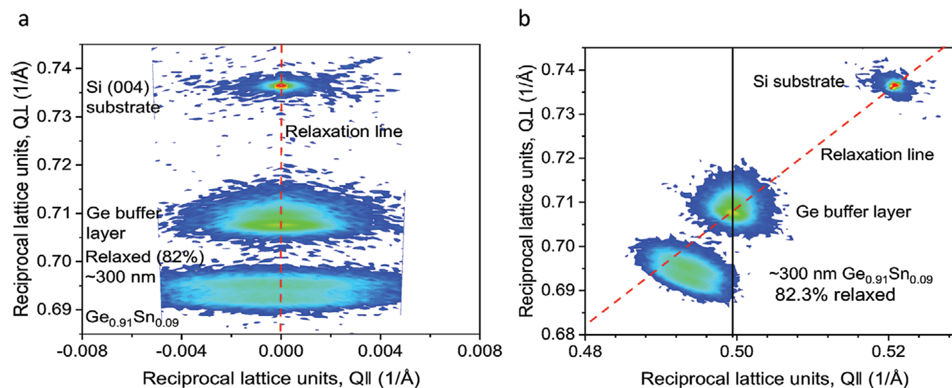

Figure 5. a) Symmetric (004) and b) asymmetric (224) HR-XRDRSMs of $Ge_{1-x}Sn_x$/Ge/Si heterostructure at 9% Sn content.

alloy as the effective mass, m^*, will increase in the alloy (see Equation 2) with Sn incorporation into the Ge, which will lead to a higher thermoelectric efficiency.

3. Conclusion

The use of alloys has proven to be a promising approach in achieving low thermal conductivity, as apparent from this study of a single crystal relaxed $Ge_{1-x}Sn_x$ binary alloy epilayers with Sn contents up to 9%. The optimization of our unique microfabrication process is essential for eliminating thermal losses and allowing the extraction of true thermal conductivity of the epilayer's material. Incorporation of α-Sn atoms into the smaller lattice constant of Ge tends to reduce the energy band gap at the Γ point.[25] It also creates crystal disorder within the alloy, and this disorder is proportional to Sn concentration. Although not verified, the crystal disorder is speculated to contribute to the increase in the phonon vibrations, resulting in low thermal conductivity. The growth of $Ge_{1-x}Sn_x$ alloy material is scalable and can be manufactured using Si-based technology, which is an advantage over the non-scalable, toxic, and expensive conventional thermoelectric materials like Bi_2Te_3, Bi_2Se_3, PbTe, etc. In contrast, $Ge_{1-x}Sn_x$ alloys exhibit enormous potential for energy generation applications by thermoelectricity at around room temperature and could be used to manufacture TE devices at low cost and mass volumes.

4. Experimental Section

The intentionally relaxed $Ge_{1-x}Sn_x$ epilayers up to ≈400 nm thick were epitaxially grown on 100 mm diameter 525 µm thick Si (001) wafers via undoped relaxed ≈600 nm thick Ge buffer layer in an industrial type ASM Epsilon 2000 reduced pressure chemical vapor deposition (RP-CVD) cold wall system.[41–43] The Si wafer was loaded into the CVD growth chamber at ≈900 °C. Then the temperature was rapidly raised up to ≈1000 °C at which native silicon oxide was thermally desorbed from the Si surface. The precursors used for the growth of $Ge_{1-x}Sn_x$ epilayers are Tin-Tetrachloride ($SnCl_4$) as Sn source, and Germane (GeH_4) as source of Ge. Purified H_2 at reduced pressure below ≈600 Torr was used as the carrier gas. Lattice mismatch between Si substrate and $Ge_{1-x}Sn_x$ epilayer was minimized by the growth of the Ge buffer layer[44]

XTEM analysis was carried out using the JEOL 2100 to measure the epilayer thicknesses of the $Ge_{1-x}Sn_x$/Ge/Si heterostructures. Types and densities of defects in the relaxed epilayers were obtained from the high-resolution TEM images and diffraction images. The micro-fabricated wires from the non-suspended $Ge_{1-x}Sn_x$/Ge/Si, suspended $Ge_{1-x}Sn_x$/Ge, and suspended single layer $Ge_{1-x}Sn_x$ epilayers were visually verified by the SEM imaging using the Supra 55 Zeiss. Suspension of both twin layers of $Ge_{1-x}Sn_x$/Ge and a single layer of $Ge_{1-x}Sn_x$ epilayers was verified by tilting the structure by 55°.

HR-XRD analysis was carried out using a Pan-analytical X'Pert Pro MRD diffractometer with CuKα radiation (λ = 0.15418 nm). Crystallographic structure of the epitaxial films of $Ge_{1-x}Sn_x$ up to 9% was examined via the ω–2Θ scan. Symmetric (004) and asymmetric (220) reciprocal space maps (RSMs) were obtained to extract information about the in-plane and out-plane lattice constants and then used to calculate Sn content and state of strain in each epilayer. Sn content in $Ge_{1-x}Sn_x$ epilayer was calculated using the following equation $a_0^{Ge_{1-x}Sn_x} = a_0^{Ge}(1-x) + a_0^{Sn}x + b^{GeSn}x(1-x)$,[44,45] with the lattice constants, a_0^{Ge} = 5.6579 Å, a_0^{Sn} = 6.4892 Å, and the bowing parameter, b^{GeSn}= 0.041 Å[45]. Sn content is represented by x. **Figure 5** shows symmetrical (004) and asymmetrical (224) HR-XRRSMs of $Ge_{1-x}Sn_x$/Ge/Si heterostructure at 9% Sn content.

Microwires were fabricated by exposure of design pattern using a Heidelberg micropattern generator, developed in an AZ326MIF developer, and etched using a mixture of H_2O_2:NH_4OH:H_2O to create $Ge_{1-x}Sn_x$/Ge/Si mesa structure . The mesa was then suspended from the substrate by an anisotropic Si wet etch process using 25% TMAH at 90 °C with an etch rate of 0.5 µm per minute, and then selectively etched to create a free-standing suspended $Ge_{1-x}Sn_x$ layer microwire. Scanning electron microscopy (SEM) was carried out to directly measure the dimensions of the fabricated microwires and to ensure their suspension. It is noted that the measured thermal conductivity from these fabricated microwires is independent of dimensions.

Thermal conductivity of the heterostructures and the individual $Ge_{1-x}Sn_x$ epilayers were obtained with the help of Raman spectroscopy via the micro-Raman thermometry of the temperature-calibrated $Ge_{1-x}Sn_x$/Ge/Si bulk samples. Raman spectra were obtained from samples at the optical excitation laser wavelength of 633 nm with a non-induced heating power density of ≈25 kW cm^{-2}[2] This is equivalent to 10% of 10 mW laser power applied, with a focused ≈1.03 µm spot size at the sample surface, through the aperture of 50× objective lens with an installed single-stage monochromator of 1800 lines mm^{-1} grating. The spectroscopy was operated at 0.3 cm^{-1} spectral resolution.

Raman thermometry measurement of $Ge_{1-x}Sn_x$ /Ge/Si epilayer was taken in vacuum between 180 and 550 K using a temperature-controlled LINKAM stage, which was monitored by a computer-based system. The sample stage was cooled down to below room temperature by liquid Nitrogen.

Thermal conductivity measurement of a thin film was usually very challenging due to the thermal influence of the substrate[34] Its measurement at the micro or nanoscale level[46,47] was demonstrated over the years using the contactless in situ Raman technique, where Raman laser acted as both the heat source and the thermometry sensor of the localized

© 2023 The Authors. Advanced Materials Interfaces published by Wiley-VCH GmbH

21967350, 0, Downloaded from https://onlinelibrary.wiley.com/doi/10.1002/admi.202300711 by Test, Wiley Online Library on [07/12/2023]. See the Terms and Conditions (https://onlinelibrary.wiley.com/terms-and-conditions) on Wiley Online Library for rules of use; OA articles are governed by the applicable Creative Commons License

ADVANCED MATERIALS INTERFACES
Open Access
www.advmatinterfaces.de

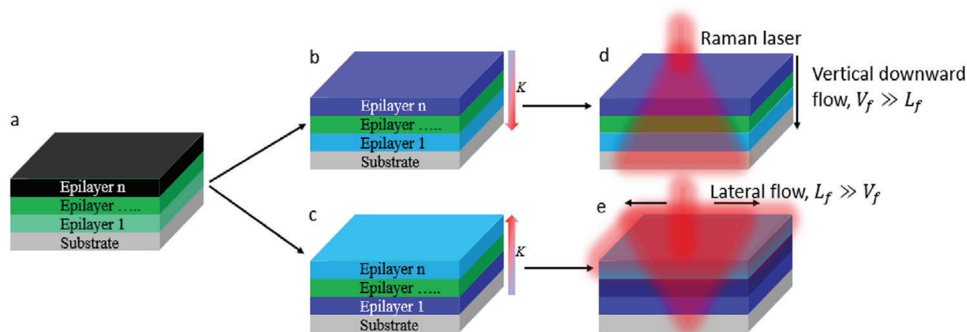

Figure 6. Thermal flow model in a) typically grown multilayer materials up to *n*th layer on substrate, b) with increasing thermal conductivity down to the substrate layer, d) demonstrating thermal diffusion toward other layer and substrate with highest thermal conductivity. c) Multilayers with decreasing thermal conductivity from *n*th layer to the substrate, e) demonstrating thermal confinement within the layer with the highest thermal conductivity.

heating effect. Obtained temperature dependence of Raman peak shift[48] from the sample could be used to determine the material's thermal conductivity. The accuracy in the thermal conductivity measurement could not be ascertained when the film's thickness was less than its substrate[34] which then becomes difficult to extract such measurement of individual thin film material. The earlier approach of the surface coating of film material to enable constriction resistance[49] requiring the substrate having higher thermal conductivity or the film material having higher thermal conductivity did not consider the thermal effect of such coating on material and had still not been found possible solutions to ensure measurement accuracy. Another approach presented[50] was to ensure that the film's thickness was higher than the laser diameter to remove the thermal effect imposed by the substrate, which thus, limits such measurements from thinner film materials. Although, a theoretical model and numerical solution[7,36,37] were presented to address these difficulties in thermal conductivity measurement of thin film material via Raman spectroscopy by thermally isolating the effect of the substrate from the film material, however, the behavior of such substrate acting as a heat sink to the film material on top was not considered as could be evidenced in a typical model of heat transfer in any multi-layer material (Figure 6).

Measurement of thermal conductivity of an epilayer material from multi-layer could either be underestimated or overestimated depending on the circumstances of other layers or substrates. In this work, first, a reliable microfabrication approach to isolate the film from either the thermal effect or strain of the buffer layer or substrate was presented. Second, the measurement model for a radial Gaussian distribution as contained in the textbook on conduction of heat in solids[35,36] was utilized in the calculation of thermal conductivity. Thermometric measurement which was responsible for the temperature-dependent vibration mode for sample surface temperature was made from relaxed bulk $Ge_{1-x}Sn_x$/Ge/Si epilayers via the in situ micro-Raman spectroscopy at 633 nm excitation laser wavelength at a non-heating power density. Assuming the surface of a material behaves isothermally, and that the Raman laser beam with a spot radius *a*, was of radial Gaussian distribution vertically down the material, the partial derivative of such surface temperature was expressed as[35]

$$\frac{\partial T}{\partial z} = f(r) = \frac{-Q}{2\pi a k (a^2 - r^2)^{1/2}}, a \geq r > 0, z = 0 \tag{5}$$

Integrating both sides gave a solution to the differential equation as contained in the book on conduction of heat in solids[35] and can be re-expressed as,

$$k = \frac{Q}{4aT} \tag{6}$$

Applied laser power density was relative to the obtained peak shift in material. The peak shift due to temperature change at the surface of material gave information about the material's temperature dependence Raman peak and could be used to measure its thermal conductivity. Considering the surface material as a perfect isothermal body, such that the laser beam (centered on the objective aperture) was a representation of radial Gaussian distribution function, the absorbed heat flux by the surface of material contained within the hemisphere under the laser beam spot can be expressed as follows[51]

$$P_{abs} = P_0 \left(1 - e^{-\frac{2r^2}{\omega^2}}\right) \tag{7}$$

The measured laser power after the objective used in the experiment is, P_0. Where, the radius of the laser spot, *r*, equals the Gaussian beam radius (beam waist), *w*, the expression becomes,

$$P_{abs} = P_0(1 - e^{-2}) = 0.865 * P_0 \tag{8}$$

Sample reflectivity of the incident laser power was measured after determining the refractive index, *n*, and the extinction coefficient, *k* as expressed as,

$$Reflectivity = (\frac{(n-1)^2 - k^2}{(n+1)^2 + k^2}) \tag{9}$$

The absorbed power density of the sample can then be expressed as follows, considering the laser spot size,

$$Q = \frac{P_{abs}}{2\pi r^2} * absorptivity = (0.865 * P_0) * (1 - (\frac{(n-1)^2 - k^2}{(n+1)^2 + k^2}) \tag{10}$$

The laser beam spot size was determined from the Airy disc approach which is dependent on the numerical aperture (NA) of the objective lens and the laser wavelength, λ, used in an experiment for measurement. For a radial Gaussian distribution of heat flux on sample, the equation representing the laser spot diameter is stated as below.

$$a = (1.22 \times \lambda)/NA \tag{11}$$

Acknowledgements

The authors thank Dr Alan Burton for the technical support of the group's equipment and facilities.

Conflict of Interest

The authors declare no conflict of interest.

© 2023 The Authors. Advanced Materials Interfaces published by Wiley-VCH GmbH

21967350, 0, Downloaded from https://onlinelibrary.wiley.com/doi/10.1002/admi.202300711 by Test, Wiley Online Library on [07/12/2023]. See the Terms and Conditions (https://onlinelibrary.wiley.com/terms-and-conditions) on Wiley Online Library for rules of use; OA articles are governed by the applicable Creative Commons License

Author Contributions

M.M. designed the experiment, developed the CVD growth technology, and prepared the epi wafers. S.A. characterized materials, fabricated the suspended structures, and characterized them. M.M. and S.A. conducted the experiment, analyzed the data, and wrote the paper.

Data Availability Statement

The data that support the findings of this study are available from the corresponding author upon reasonable request.

Keywords

CVD, epitaxy, germanium tin, microfabrication, thermal conductivity

Received: August 27, 2023
Revised: October 17, 2023
Published online:

[1] P. D. Maycock, *Solid-State Electron.* **1967**, *10*, 161.
[2] X. Tang, Z. Li, W. Liu, Q. Zhang, C. Uher, *Interdiscip. Mater.* **2022**, *1*, 88.
[3] J. Mao, Z. Liu, J. Zhou, H. Zhu, Q. Zhang, G. Chen, Z. Ren, *Adv. Phys.* **2018**, *67*, 69.
[4] H. Zhu, J.-Y. Zhao, C. Xiao, *Rare Met.* **2021**, *40*, 2829.
[5] B. Qin, D. Wang, X. Liu, Y. Qin, J.-F. Dong, J. Luo, J.-W. Li, W. Liu, G. Tan, X. Tang, J.-F. Li, J. He, L.-D. Zhao, *Science* **2021**, *373*, 556.
[6] S. N. Khatami, Z. Aksamija, *Phys. Rev. Appl.* **2016**, *6*, 014015.
[7] D. Spirito, N. von den Driesch, C. L. Manganelli, M. H. Zoellner, A. A. Corley-Wiciak, Z. Ikonic, T. Stoica, D. Grützmacher, D. Buca, G. Capellini, *ACS Appl. Energy Mater.* **2021**, *4*, 7385.
[8] Z.-H. Zheng, X.-L. Shi, D.-W. Ao, W.-D. Liu, M. Li, L.-Z. Kou, Y.-X. Chen, F. Li, M. Wei, G.-X. Liang, *Nat. Sustain.* **2022**, *6*, 180.
[9] Q. Yan, M. G. Kanatzidis, *Nat. Mater.* **2022**, *21*, 503.
[10] D. M. Rowe, *Thermoelectrics handbook: macro to nano*, CRC Press, Taylor & Francis Group **2018**.
[11] G. J. Snyder, E. S. Toberer, *Materials for sustainable energy: a collection of peer-reviewed research and review articles from*, Nature Publishing Group, World Scientific **2011**, pp. 101.
[12] Z. Chen, Z. Jian, W. Li, Y. Chang, B. Ge, R. Hanus, J. Yang, Y. Chen, M. Huang, G. J. Snyder, Y. Pei, *Adv. Mater.* **2017**, *29*, 1606768.
[13] C. W. Li, J. Hong, A. F. May, D. Bansal, S. Chi, T. Hong, G. Ehlers, O. Delaire, *Nat. Phys.* **2015**, *11*, 1063.
[14] D. Bansal, J. Hong, C. W. Li, A. F. May, W. Porter, M. Y. Hu, D. L. Abernathy, O. Delaire, *Phys. Rev. B* **2016**, *94*, 054307.
[15] B. Jiang, Y. Yu, H. Chen, J. Cui, X. Liu, L. Xie, J. He, *Nat. Commun.* **2021**, *12*, 1.
[16] Y. Pei, H. Wang, G. Snyder, *Adv. Mater.* **2012**, *24*, 6124.
[17] T. Hong, D. Wang, B. Qin, X. Zhang, Y. Chen, X. Gao, L.-D. Zhao, *Mater. Today Phys.* **2021**, *21*, 100505.
[18] M. Ogura, D. Han, M. M. Pointner, L. S. Junkers, S. S. Rudel, W. Schnick, H. Ebert, *Phys. Rev. Mater.* **2021**, *5*, 024601.
[19] Z. Charifi, H. Baaziz, B. Hamad, *Phys. B* **2009**, *404*, 1632.
[20] Y. Chibane, M. Ferhat, *J. Appl. Phys.* **2010**, *107*, 053512.
[21] Y. Gul, M. Myronov, S. N. Holmes, M. Pepper, *Phys. Rev. Appl.* **2020**, *14*, 054064.
[22] C. Claeys, H. Arimura, N. Collaert, J. Mitard, R. Rooyackers, E. Simoen, A. Vandooren, A. Veloso, N. Waldron, L. Witters, *Phys. Status Solidi A* **2016**, *213*, 2820.
[23] L. I. Berger, *Semiconductor materials*, CRC Press, Taylor & Francis, London **1996**.
[24] M. Myronov, A. Dobbie, V. A. Shah, X.-C. Liu, V. H. Nguyen, D. R. Leadley, *Electrochem. Solid-State Lett.* **2010**, *13*, H388.
[25] S. Wirths, R. Geiger, N. Von Den Driesch, G. Mussler, T. Stoica, S. Mantl, Z. Ikonic, M. Luysberg, S. Chiussi, J.-M. Hartmann, *Nature Photon.* **2015**, *9*, 88.
[26] D. Gerthsen, D. K. Biegelsen, F. A. Ponce, J. C. Tramontana, *J. Cryst. Growth* **1990**, *106*, 157.
[27] F. Pezzoli, A. Giorgioni, D. Patchett, M. Myronov, *ACS Photonics* **2016**, *3*, 2004.
[28] V. A. Shah, A. Dobbie, M. Myronov, D. R. Leadley, *Solid-State Electron.* **2011**, *62*, 189.
[29] V. A. Shah, A. Dobbie, M. Myronov, D. R. Leadley, *Thin Solid Films* **2011**, *519*, 7911.
[30] U. Holzwarth, N. Gibson, *Nat. Nanotechnol.* **2011**, *6*, 534.
[31] J. R. Watling, D. J. Paul, *J. Appl. Phys.* **2011**, *110*, 114508.
[32] J. Zheng, Z. Liu, Y. Zhang, Y. Zuo, C. Li, C. Xue, B. Cheng, Q. Wang, *J. Cryst. Growth* **2018**, *492*, 29.
[33] C. L. Manganelli, M. Virgilio, O. Skibitzki, M. Salvalaglio, D. Spirito, P. Zaumseil, Y. Yamamoto, M. Montanari, W. M. Klesse, G. Capellini, *J. Raman Spectrosc.* **2020**, *51*, 989.
[34] H. Scherrer, S. Scherrer, D. Rowe, *Thermoelectrics Handbook: Macro to Nano*, CRC, Boca Raton **2006**.
[35] H. S. Carslaw, J. C. Jaeger, *Conduction of heat in solids*, Oxford, **1947**, p. 71.
[36] D. Xu, Y. Sang, Y. Chu, Y. Yu, F. Liu, Y. Hou, X. Wang, *Mater. Res. Express* **2021**, *8*, 056403.
[37] N. M. Wight, E. Acosta, R. K. Vijayaraghavan, P. J. Mcnally, V. Smirnov, N. S. Bennett, *Therm. Sci. Eng. Prog.* **2017**, *3*, 95.
[38] Y. Jiang, J. Dong, H.-L. Zhuang, J. Yu, B. Su, H. Li, J. Pei, F.-H. Sun, M. Zhou, H. Hu, J.-W. Li, Z. Han, B.-P. Zhang, T. Mori, J.-F. Li, *Nat. Commun.* **2022**, *13*, 6087.
[39] A. Portavoce, H. Khelidj, N. Oueldna, S. Amhil, M. Bertoglio, D. Mangelinck, L. Essaleh, K. Hoummada, *Materialia* **2020**, *14*, 100873.
[40] M. Kurosawa, O. Nakatsuka, *ECS Trans.* **2021**, *104*, 183.
[41] E. Rogowicz, J. Kopaczek, J. Kutrowska-Girzycka, M. Myronov, R. Kudrawiec, M. Syperek, *ACS Appl. Electron. Mater.* **2021**, *3*, 344.
[42] E. Vitiello, S. Rossi, C. A. Broderick, G. Gravina, A. Balocchi, X. Marie, E. P. O'reilly, M. Myronov, F. Pezzoli, *Phys. Rev. Appl.* **2020**, *14*, 064068.
[43] R. Millar, D. Dumas, K. Gallacher, P. Jahandar, C. MacGregor, M. Myronov, D. Paul, *Opt. Express* **2017**, *25*, 25374.
[44] P. Jahandar, D. Weisshaupt, G. Colston, P. Allred, J. Schulze, M. Myronov, *Semicond. Sci. Technol.* **2018**, *33*, 034003.
[45] S. Wirths, D. Buca, S. Mantl, *Prog. Cryst. Growth Charact. Mater.* **2016**, *62*, 1.
[46] M. Li, C. Li, J. Wang, X. Xiao, Y. Yue, *Appl. Phys. Lett.* **2015**, *106*, 253108.
[47] A. Ould-Abbas, M. Bouchaour, N.-E. C. Sari, Study of thermal conductivity of porous silicon using the micro-raman method, **2012**.
[48] T. R. Hart, R. L. Aggarwal, B. Lax, *Phys. Rev. B* **1970**, *1*, 638.
[49] J. Dryden, The effect of a surface coating on the constriction resistance of a spot on an infinite half-plane, **1983**.
[50] S. Périchon, V. Lysenko, B. Remaki, D. Barbier, B. Champagnon, *J. Appl. Phys.* **1999**, *86*, 4700.
[51] A. E. Siegman, Lasers. University science books, **1986**.

© 2023 The Authors. Advanced Materials Interfaces published by Wiley-VCH GmbH

21967350, 0, Downloaded from https://onlinelibrary.wiley.com/doi/10.1002/admi.202300711 by Test, Wiley Online Library on [07/12/2023]. See the Terms and Conditions (https://onlinelibrary.wiley.com/terms-and-conditions) on Wiley Online Library for rules of use; OA articles are governed by the applicable Creative Commons License